



American Society of
Mechanical Engineers

ASME Accepted Manuscript Repository

Institutional Repository Cover Sheet

Michele Sergio

First

Campobasso

Last

ASME Paper Title: Assessing the Sensitivity of Stall-Regulated Wind Turbine Power to Blade Design Using

High-fidelity CFD

Authors: A.G. Sanvito, G. Persico, M.S. Campobasso

ASME Journal Title: Journal of Engineering for Gas Turbines and Power

Volume/Issue 141(10)

Date of Publication (VOR* Online) 24 September 2019

ASME Digital Collection URL:

<https://asmedigitalcollection.asme.org/gasturbinespower/article-abstract/141/10/101022/975413/Assessing-the-Sensitivity-of-Stall-Regulated-Wind?redirectedFrom=fulltext>

DOI: 10.1115/1.4044731

ASME ©; CC-BY distribution license

*VOR (version of record)

Assessing the Sensitivity of Stall-Regulated Wind Turbine Power to Blade Design Using High-fidelity CFD

Andrea G. Sanvito

Research Student

Politecnico di Milano

Dipartimento di Energia

Via Lambruschini 4

20156-Milano, Italy

andreagiuseppe.sanvito@mail.polimi.it

Giacomo Persico

Associate Professor

Politecnico di Milano

Dipartimento di Energia

Via Lambruschini 4

20156-Milano, Italy

giacomo.persico@polimi.it

M. Sergio Campobasso*

Associate Professor

University of Lancaster, Department of Engineering

Engineering Building, Gillow Avenue

Lancaster LA1 4YR, United Kingdom

m.s.campobasso@lancaster.ac.uk

ABSTRACT

This study provides a novel contribution towards the establishment of a new high-fidelity simulation-based design methodology for stall-regulated horizontal axis wind turbines. The aerodynamic design of these machines is complex, due to the difficulty of reliably predicting stall onset and post-stall characteristics. Low-fidelity design methods, widely used in industry, are computationally efficient, but are often affected by significant uncertainty. Conversely, Navier-Stokes CFD can reduce such uncertainty, resulting in lower development costs by reducing the need of field testing of designs not fit for purpose. Here, the compressible CFD research code COSA is used to assess the performance of two alternative designs of a 13-meter stall-regulated rotor over a wide range of operating conditions. Validation of the numerical methodology is based on thorough comparisons of novel simulations and measured data of the NREL Phase VI turbine rotor, and one of the two industrial rotor designs. An excellent

*Corresponding author.

agreement is found in all cases. All simulations of the two industrial rotors are time-dependent, to capture the unsteadiness associated with stall which occurs at most wind speeds. The two designs are cross-compared, with emphasis on the different stall patterns resulting from particular design choices. The key novelty of this work is the CFD-based assessment of the correlation among turbine power, blade aerodynamics, and blade design variables (airfoil geometry, blade planform and twist) over most operational wind speeds.

INTRODUCTION

Distributed power generation based on small wind turbines (SWTs) is rapidly gaining technical and economic relevance, with a strong commercial potential, not only for application in clean and smart cities, but also for the growing demand of clean electricity in remote areas not served by the grid, both in developed and developing countries. In 2015 the SWT power capacity installed worldwide exceeded 750 MW, with 40% of such capacity in China, 25% in the United States and 15% in the United Kingdom, and the annual growth rate of SWTs at the end of 2013 was 8% [1]. The detailed SWT cost analyses of [2] show that the initial investment (turbine and installation costs) is the main cost driver of SWT power plants, ranging from 7,600 to 1,700 €/kWh as the rated power increases from 2.5 to 200 kW. Interested readers are referred to [2] for further detail on SWT cost and viability analyses.

Passive-control horizontal axis wind turbines (HAWTs) play a key role in the SWT arena, due to their relatively low capital and maintenance costs. The aerodynamics of such machines, however, is complex due to relatively low Reynolds numbers, large variations of the relative flow speed from blade root to tip, and the occurrence of stall. All this makes the design of these machines a challenging task. The design of small stall-regulated HAWTs is the main focus of this study, which provides a new contribution to the high-fidelity simulation-based design methodology of this turbine type.

HAWT aerodynamic design is still based overwhelmingly on semi-analytical methods, such as the blade element momentum theory (BEMT) [3], and experienced designers' judgment. BEMT codes are computationally efficient, but unfortunately their results may be affected by significant uncertainty due to the use of semi-empirical correlation-based models. Conversely, the use of three-dimensional (3D) Reynolds-Averaged Navier-Stokes (RANS) Computational Fluid Dynamics (CFD) codes for HAWT aerodynamics [4–7] can reduce the aforementioned uncertainty [8], since this approach is largely based on first principles. CFD often requires relatively large computing resources, but cheaper cloud computing and ongoing innovation in high-performance computing hardware is reducing this burden.

The aerodynamic design of stall-regulated HAWTs is a particularly challenging task, due to the difficulty of reliably predicting stall onset, and the aerodynamic performance of stalled airfoils in the post-stall regime. CFD has been used extensively for validation purposes to analyze the aerodynamic performance of small research rotors, such as those of the National Renewable Energy Laboratory (NREL) Phase VI turbine [9] and the Model Experiments in Controlled Conditions (MEXICO) turbine [10]. However, the potential of this high-fidelity simulation technology to improve small-scale HAWT design in terms of both performance and reliability of the design outcome has yet to be demonstrated. High-fidelity CFD-based design can also reduce product development costs with respect to common low-fidelity design methods by reducing the need of field testing rotors which might eventually be discarded due to unexpectedly poor measured performance.

One of the few examples of introducing CFD in the design cycle of small HAWT rotors is provided in [11], which used incompressible flow ANSYS FLUENT simulations to verify the design of a 3 meter-diameter turbine. In the present study, the impact of high-fidelity CFD on the design of small commercial HAWTs is demonstrated by using the compressible RANS finite volume code COSA [12] to assess the aerodynamic characteristics and power output of two alternative configurations of a 13-meter stall-regulated commercial HAWT over a wide range of operational wind speeds. COSA uses Menter's Shear Stress Transport (SST) turbulence model [13] and a novel efficient and accurate low-speed preconditioner to maximize solution quality and convergence speed of low-Mach problems [14]. One of the key original elements of this work is the CFD-based assessment of the correlation between turbine power and key blade design variables, such as airfoil characteristics, blade platform and twist, over most operational wind speeds.

The paper is structured as follows. The governing equations are presented first, and this is followed by a description of the CFD solver, and a brief discussion of the low-speed preconditioner in COSA. A novel validation study based on the comparison of new COSA results and measured data of the flow field of the NREL Phase VI rotor for freestream wind speed of 7 m/s is then presented before the result section, which focusses on the comparative assessment of two design alternatives for a commercial 13-meter stall-regulated HAWT rotor. The concluding section summarizes the main findings of the study.

GOVERNING EQUATIONS

The compressible RANS equations are obtained by time-averaging the compressible NS equations on the turbulence time-scales, and form a system of conservation laws expressing the conservation of mass, momentum and energy of mean viscous fluid flows time-averaged on abovesaid turbulence time-scales. The RANS equations are formally similar to the NS equations but feature an additional symmetric tensor depending on the time-averages of six distinct pairs of velocity component fluctuations. This term, known as Reynolds stress tensor, accounts in a mean fashion for the effects of turbulence on the sought mean flow field, and, making use of Boussinesq's approximation, it can be expressed as the product of an eddy viscosity and the strain rate tensor based on the mean velocity field. In the COSA CFD code used in this study, the former variable is computed with the two-equation $k - \omega$ SST turbulence model. Thus, turbulent compressible flows are determined by solving a system of seven partial differential equations (PDEs) and an equation of state linking fluid density, pressure and internal energy.

In many applications involving rotational body motion (*e.g.* turbomachinery, helicopter and HAWT rotor flows), it is convenient to formulate the governing equations in a rotating frame of reference, since, in the absence of external aerodynamic forcing and aerodynamic instabilities, this enables solving a problem that is unsteady in the stationary frame as a steady-state problem in the rotating frame. Using this approach, the grid position is fixed during the analysis. When formulating the governing equations in the rotating frame, one can express the unknown fluid velocity vector and all terms depending on said velocity by using either the relative or the absolute velocity components. The two formulations are mathematically equivalent [15], but using a representation of the relative fluid velocity based on the absolute components is numerically more convenient for open rotor applications. Therefore, in COSA the unknown flow velocity components are the absolute ones at an arbitrary time, even though the conservation laws are expressed in the rotating frame.

The Arbitrary Lagrangian–Eulerian (ALE) integral form of the system of the time–dependent RANS and SST equations is written in a Cartesian coordinate system rotating about the z axis with constant angular velocity $\underline{\Omega}$, and with the y axis being the blade stacking line. Given a control volume C with boundary S in the considered rotating frame, the ALE integral form of the system of time–dependent RANS and SST equations is:

$$\frac{\partial}{\partial t} \left(\int_C \mathbf{U} dC \right) + \oint_S (\underline{\Phi}_c - \underline{\Phi}_d) \cdot d\underline{S} - \int_C \mathbf{S}_r dC = 0 \quad (1)$$

where $\mathbf{U} = [\rho \quad \rho \underline{\mathbf{u}}^T \quad \rho E \quad \rho k \quad \rho \omega]^T$ is the array of conservative variables, the superscript T denotes the transpose operator, and the symbols ρ , $\underline{\mathbf{u}}$, E , k and ω denote respectively density, absolute velocity vector, total energy, turbulent kinetic energy and specific dissipation rate of turbulent kinetic energy per unit mass. The velocity vector $\underline{\mathbf{u}}$ has Cartesian components (u, v, w) . The total energy is $E = e + (\underline{\mathbf{u}} \cdot \underline{\mathbf{u}})/2 + k$, where e denotes the internal energy per unit mass and $(\underline{\mathbf{u}} \cdot \underline{\mathbf{u}})/2$ is the mean flow kinetic energy per unit mass [12]; the perfect gas model is used to express the static pressure p as a function of ρ , e . The generalized convective flux vector $\underline{\Phi}_c$ is:

$$\underline{\Phi}_c = \begin{bmatrix} \rho(\underline{\mathbf{u}} - \underline{\mathbf{u}}_b)^T \\ \rho(\underline{\mathbf{u}} - \underline{\mathbf{u}}_b)^T \underline{\mathbf{u}} + pI \\ \rho E(\underline{\mathbf{u}} - \underline{\mathbf{u}}_b)^T + p \underline{\mathbf{u}}^T \\ \rho k(\underline{\mathbf{u}} - \underline{\mathbf{u}}_b)^T \\ \rho \omega(\underline{\mathbf{u}} - \underline{\mathbf{u}}_b)^T \end{bmatrix} \quad (2)$$

where I is the (3×3) identity matrix, $\underline{\mathbf{u}}_b$ is the boundary velocity (i.e., the entrainment velocity at the points of the boundary S of the control volume), and $(\underline{\mathbf{u}} - \underline{\mathbf{u}}_b)$ can be viewed as the relative fluid velocity. The boundary velocity $\underline{\mathbf{u}}_b$ is given by:

$$\underline{\mathbf{u}}_b = \underline{\Omega} \times \underline{\mathbf{r}} \quad (3)$$

in which $\underline{\mathbf{r}}$ denotes the position vector in the rotating frame. The definition of the generalized diffusive flux vector $\underline{\Phi}_d$ is reported in [12], and the source term \mathbf{S}_r is given by:

$$\mathbf{S}_r = [0 \quad -\rho \Omega v \quad \rho \Omega u \quad 0 \quad 0 \quad S_k \quad S_\omega]^T \quad (4)$$

where Ω denotes the modulus of $\underline{\Omega}$, and S_k and S_ω denote respectively the source terms of the k and ω equations of the SST

turbulence model. The definitions of S_k and S_ω are provided in [12].

CFD SOLVER

The structured multi-block compressible RANS code COSA used in this project solves System (1) using a cell centered finite volume discretization. The code was successfully used to investigate the unsteady hydrodynamics of oscillating wings to extract energy from an oncoming fluid stream [12, 16, 17], and the unsteady aerodynamics of Darrieus vertical axis wind turbines [18–20], fixed-bottom HAWTs in yawed wind [21], and floating offshore wind turbines subject to tower pitching [22].

The discretization of the convective fluxes of both the RANS and the SST PDEs is based on Van Leer’s second order *MUSCL* extrapolations, Roe’s flux-difference splitting (FDS), and Van Albada’s flux limiter. The code can also use a third order accurate discretization of the convective fluxes based on third order *MUSCL* extrapolations, Roe’s FDS, and Venkatakrishnan’s flux limiter [23]. The discretization of all diffusive fluxes and all source terms of the SST model involving velocity derivatives is based on second order central differencing [12, 16]. In rotor flow analyses, the cell face velocities \underline{u}_b in Eq. (2) are computed using the freestream–capturing geometric relations of [24] to ensure global conservation. It should be noted that both the source terms depending on Ω in Eq. (4) and the cell face velocities \underline{u}_b are nonzero also for steady rotor flows. Further detail on the freestream–capturing discretization of \underline{u}_b is available in [22].

The integration of the steady RANS and SST equations is performed in a strongly-coupled fashion [12] using explicit Runge–Kutta time–marching, with local time–stepping, implicit residual smoothing and multigrid for convergence acceleration. Time-dependent problems are solved using Jameson’s second–order dual–time stepping [12, 16]. To illustrate the general integration process of COSA, it is convenient to consider the semi–discrete form of System (1) adapted to Runge–Kutta (RK) cycling, *i.e.* the equation obtained by space-discretizing all flux and source terms, and adding a fictitious time-derivative for pseudo-time-marching. For a particular grid cell, such equation reads:

$$\frac{d\mathbf{Q}}{d\tau}V + \mathbf{R}(\mathbf{Q}) = 0 \quad (5)$$

where V denotes the cell volume, \mathbf{Q} is the array of conservative variables (*i.e.* the discrete counterpart of array \mathbf{U} in System (1)), $\mathbf{R}(\mathbf{Q})$ is the residual array resulting from the balance of convective and diffusive fluxes over the cell faces and all source terms over the cell volume, and $d\mathbf{Q}/d\tau$ is a fictitious time-derivative. Steady problems are solved by discretizing the fictitious time-derivative with a four-stage RK scheme and time–marching to the sought stationary state; the flow field at each physical time of time–dependent problems is obtained with the same approach, incorporating in the residual array also the discrete counterpart of the time–derivative in System (1).

COSA also features an efficient harmonic balance (HB) solver [25–27] for the rapid solution of periodic rotor flows, which was shown to reduce by up to 50 times the runtime of the NS CFD analysis of HAWT rotors with respect to the conventional time–domain method [21]. COSA has a highly efficient distributed memory (MPI) parallelization of both its

computing and IO sections [28], and has a hybrid architecture for concurrent distributed- and shared-memory computing enabling an optimal exploitation of new multi- and many-core processors [29].

LOW-SPEED PRECONDITIONING

The solution accuracy of density-based CFD codes like COSA decreases in the presence of low-speed flow regions where the local Mach number drops below the threshold of 0.1 [16]. This is due primarily to improper scaling of the numerical dissipation components as the local Mach number tends to zero. When solving the density-based compressible flow equations using iterative integration methods with a CFL constraint such as the Runge–Kutta smoother used by COSA, low flow speeds also result in a significant reduction of the solution convergence rate. In inviscid and, to a significant extent, also in high-Reynolds number flows, this occurs because of the large disparity of acoustic and convective speeds. Low-speed preconditioning (LSP) [30] can resolve the accuracy issue by restoring the balance of all terms appearing in the matrix-valued numerical dissipation in the incompressible flow limit, and can also improve the convergence rate of iterative solvers by reducing the disparity of acoustic and convective speeds. Indeed, the re-equalization of the characteristic speeds yields convergence rates which, for inviscid and relatively simple viscous flow problems, are fairly independent of the Mach number [16].

The use of LSP in the integration process of COSA results in the appearance of a preconditioning matrix $(\Gamma_c)^{-1}$ pre-multiplying the fictitious time-derivative of Eq. (5), which thus becomes:

$$(\Gamma_c)^{-1} \frac{d\mathbf{Q}}{d\tau} V + \mathbf{R}(\mathbf{Q}) = 0 \quad (6)$$

It is noted that for time-dependent problems the preconditioner does not destroy the time-accuracy of the unsteady solution because the physical time-derivatives are included in the residual array $\mathbf{R}(\mathbf{Q})$ and are therefore unaffected by the preconditioner once the iterative solution process has converged and the fictitious time-derivative vanishes. For both steady and time-dependent problems, LSP improves the solution quality at low flow speeds due to re-scaling of the numerical dissipation [14] incorporated in $\mathbf{R}(\mathbf{Q})$; LSP also improves the solution convergence rate, a benefit achieved by using the eigenvalues of the preconditioned convective flux Jacobian to calculate the local time-step for pseudo-time-marching.

The COSA LSP algorithm was designed and implemented starting from the preconditioner proposed by Weiss and Smith [31]. One of the unique and novel features of the LSP algorithm implemented in COSA [14] is that it is applied to both the RANS and SST equations, a feature required for using the computationally efficient strongly coupled integration of the two sets of equations also for problems containing low-speed regions.

Although compressibility effects in existing small and utility-scale HAWTs flows are relatively small and limited to the outboard blade sections [32], the compressible flow formulation was adopted in COSA to make the code suitable for the widest possible range of wind energy applications. In particular, significant compressible flow effects are known to occur in a) new large utility-scale rotors, which will have tip Mach numbers closer to or possibly above the incompressible limit

of 0.3, and *b*) floating off-shore wind turbines, in which the Mach number of the relative air speed past the rotor blades can be well above 0.3 due to the tower entrainment velocity [22]. In these HAWT applications a compressible flow simulation is required for reliably resolving the compressible flow regions past the blades, whereas LSP is required to deal with the remaining regions where the local relative speeds can have Mach numbers of 0.01 or lower.

VALIDATION

The second order accuracy of both space– and time–discretizations of COSA, and the code’s predictive capabilities were demonstrated in [12, 16, 25, 26, 33]. To assess the predictive capabilities of the LSP–enhanced COSA code for complex wind turbine flows like those of the industrial HAWT rotors examined in the Results section, one of the NREL Phase VI wind turbine test cases [9] is considered herein. The flow field past the selected upwind rotor in straight wind is computed using the LSP–enhanced code and compared with detailed experimental measurements. It is noted that the NREL Phase VI test case analyzed herein is the same analyzed in [21], but the COSA analyses therein were performed without LSP. In that study, the solution quality reduction due to using a density–based code without LSP was prevented by increasing the freestream velocity, and altering the fluid viscosity and rotor speed so as to maintain the same tip–speed–ratio and the same Reynolds number of the experiment. The LSP–approach presented herein is more general and robust, and the novel analyses of this section demonstrate for the first time the success and viability of the COSA strongly coupled LSP method [14] for wind turbine aerodynamics.

In section Results, the validation of the adopted numerical method is enriched by a comparison of computed and measured power data of one of the examined industrial rotor designs. This type and level of validation is paramount to the considered engineering application, since small stall–regulated turbines exhibit specific aerodynamic features whose assessment requires accurate investigation approaches, validated against experiments.

The NREL Phase VI rotor has two blades, radius $R = 5.029$ m, linear chord and nonlinear twist distributions along the blade; in the test considered, the blades have tip pitch of 3° towards feather, and the rotor has no coning. This stall–regulated turbine has rated power of 19.8 kW and freestream wind speed u_∞ of 6 m/s at cut-in. The considered operating condition has $u_\infty = 7$ m/s, oncoming air density $\rho = 1.246$ kg/m³ and dynamic viscosity $\mu = 1.769 \times 10^{-5}$ kg/ms.

In the CFD simulations, only the rotor was modeled and zero wind shear was assumed. Figure 1 reports views of the blade geometry and the 180° grid sector used for the steady simulations. The dimensions of the physical domain and the boundary conditions (BCs) applied to its boundaries are also illustrated. The hub was modeled as a short zero–thickness cylindrical surface, and an inviscid wall BC was used on its inner and outer sides, as depicted in the top left plot of Fig. 1. The blade tip was modeled using a sharp cut.

Calculations were performed with two meshes. A “fine” grid was obtained by discretizing the blade airfoils with 256 mesh intervals and the blade length with 128 spanwise intervals, adding another 96 intervals from the tip to the cylindrical far field boundary. The fine grid has about 17.0 M cells; the distance d_w of the first grid points off the blade surface from the blade surface itself is about $1 \cdot 10^{-5}c$, where c is the local airfoil chord, and this choice makes the nondimensionalized wall distance y^+ less than 1 on the whole blade surface. For grid–dependence analyses, a “coarse” grid was obtained from the

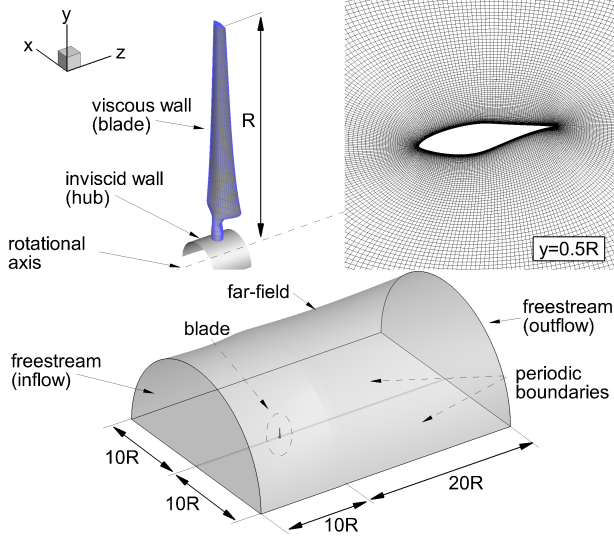


Fig. 1. NREL Phase VI HAWT: blade geometry (top left), airfoil grid at 50 % tip radius (top right), and domain dimensions and boundary conditions (bottom).

fine by removing every second line in all three directions, yielding a grid with 2.1 M cells. Further detail of these two grids is available in [34].

Measured and computed profiles of normal force coefficient C_N and tangential force coefficient C_T along the blade span are compared in the top and bottom plots of Fig. 2 respectively. The profiles labelled 'LSP coarse' and 'LSP fine' refer respectively to the CFD simulations using the LSP-enhanced code with coarse and fine grids, whereas those labelled 'NP coarse' and 'NP fine' were obtained using the baseline code. In all cases, the freestream Mach number is identical to that of the experiment. The definitions of C_N and C_T are respectively:

$$C_N = \sum_{i=1}^{n_s} \left(\frac{c_{p_i} + c_{p_{i+1}}}{2} \right) (x'_{i+1} - x'_i) \quad (7)$$

$$C_T = \sum_{i=1}^{n_s} \left(\frac{c_{p_i} + c_{p_{i+1}}}{2} \right) (y'_{i+1} - y'_i) \quad (8)$$

where x' and y' are respectively the coordinates along and normal to the airfoil chord, n_s is the number of mesh intervals along the airfoils in the CFD estimates, and the number of pressure taps in the experimental set-up, and c_p is the local static pressure coefficient. The definition of c_p is:

$$c_p = \frac{p^a - p_\infty}{\frac{1}{2}\rho_\infty [u_\infty^2 + (\Omega r)^2]} \quad (9)$$

where p^a and p_∞ denote respectively airfoil and freestream static pressure, and r is the radial position along the blade.

Figure 2 highlights that coarse- and fine-grid LSP results are close to each other, and well within the uncertainty range of the experimental data at all five radial positions where the blade static pressure was measured in the experiment. The largest

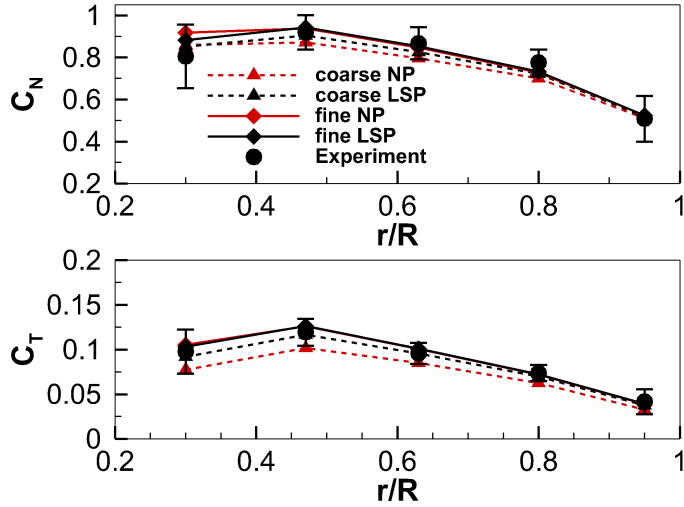


Fig. 2. NREL Phase VI HAWT: measured and computed spanwise profiles of normal force coefficient C_N (top) and tangential force coefficient C_T (bottom) for $u_\infty = 7$ m/s.

differences between measured and computed profiles occur on the lower radii, but both LSP solutions remain within the range of measurement uncertainty. Conversely, the coarse- and fine-grid force profiles computed without LSP, particularly so the tangential force coefficient, differ substantially more than their LSP counterparts. One sees that the fine-grid solutions obtained with and without LSP differ fairly little, whereas the coarse-grid force profiles differ by a much greater extent. This occurs because of the unbalanced amount of numerical dissipation of the code without LSP, and because the overall amount of numerical dissipation decreases as the mesh refinement increases. These observations also highlight that the use of LSP enables computing accurate solutions making use of a lower mesh refinement than a code without LSP would require. Thus using LSP results in large computational savings, an occurrence paramount to boosting the deployment of CFD for industrial wind turbine design.

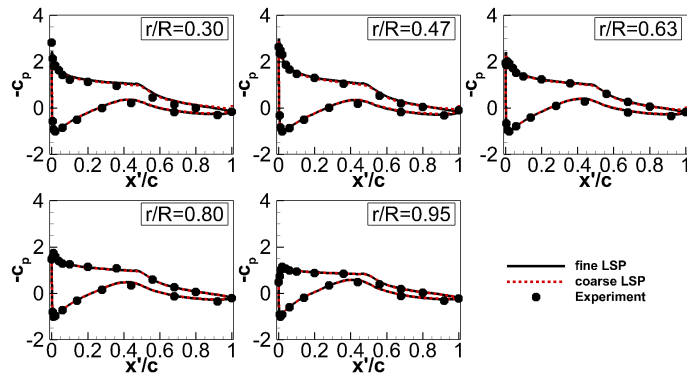


Fig. 3. NREL Phase VI HAWT: measured and computed blade pressure coefficient c_p at five radial positions for $u_\infty = 7$ m/s.

The excellent agreement of LSP-enhanced COSA solutions and experimental measurements correspond to a similar level of agreement of measured and computed chordwise profiles c_p at the five radial positions where the blade static pressure was measured, as shown in Fig. 3. The simulations with both coarse and fine grids capture quantitatively and qualitatively

Table 1. NREL Phase VI HAWT: measured and computed thrust F_z and torque M_z of one blade for $u_\infty = 7$ m/s.

	COSA coarse		COSA fine		experiment	
	$F_z(N)$	$M_z(Nm)$	$F_z(N)$	$M_z(Nm)$	$F_z(N)$	$M_z(Nm)$
LSP	548.3	358.2	563.5	364.5	578.5	402.0
NP	547.0	339.2	564.0	363.7	578.5	402.0

the experimental measurements, particularly the significant leading edge loading of the first three sections, the region of adverse pressure gradients on the pressure side of the blade, and the slope discontinuity on the suction side at $x/c \approx 0.5$.

Measured values of thrust F_z and torque M_z on one blade are compared to coarse- and fine-grid CFD results obtained with and without LSP in Tab. 1. Differences of less than 3% are found between coarse- and fine-grid LSP-enhanced predictions of thrust and torque. The fine-grid thrust prediction is closer to the experimental value (3% difference) than the coarse-grid value, which differs by about 5% from the measured thrust. It is observed that the use of LSP significantly improves the fine-grid solution compared to the numerical results of [21], which were obtained without LSP by increasing the freestream Mach number, as explained above. The coarse-grid torque prediction of the LSP solution is about 10% lower than the measured value, and only a marginal improvement is achieved with the fine grid. This level of agreement, however, is comparable with that reported in the literature and is within the uncertainty range of the torque measurements [35]. The comparison of the values of F_z and M_z obtained with the coarse- and fine-grid simulations without LSP and the other data in Table 1 is consistent with the results in Fig. 2, highlighting that the coarse-grid LSP-code torque prediction is significantly closer to the measured value than that of the code without LSP using the same coarse grid.

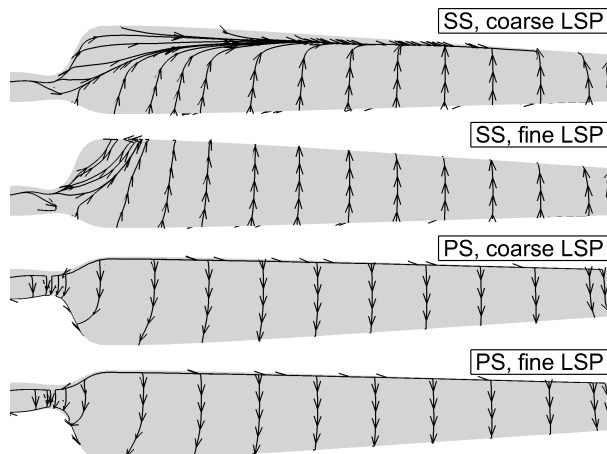


Fig. 4. NREL Phase VI HAWT: limiting streamlines on suction and pressure side of coarse- and fine-grid LSP solutions for $u_\infty = 7$ m/s.

Inspection of the limiting streamlines on the two surfaces of the blade in Figure 4 highlights some local differences between the coarse- and fine-grid predictions of the LSP-enhanced code. The coarse-mesh solution indicates that flow separation on the suction side occurs over most of the blade height, and the separation point moves towards the trailing edge as the radius increases. This flow pattern is absent in the fine-mesh solution, which predicts flow separation only in the

blade root region, limited to the first 15% of the blade length. These patterns are reflected in the c_p profiles of Fig. 3. The coarse-grid simulation slightly underpredicts the suction side pressure recovery at $r/R = 0.3$ and $r/R = 0.47$ for $x/c > 0.9$ with respect to the fine-mesh prediction, which instead is in very good agreement with the measured trailing edge pressure. These phenomena also explain the observed small differences in the coarse- and fine-grid predictions of the force coefficients along the blade, which, however, are very small with respect to the experimental uncertainty.

The simulations discussed above are fully turbulent. The boundary layers were not tripped at the leading edge during the experiment. At the low level of turbulence intensity of about 0.5% at which the experiment was carried out, and due to the very smooth state of the blade surfaces, laminar-to-turbulent transition is likely to occur on the blade suction surfaces. Sørensen's comparison of fully turbulent and transitional CFD results for the operating consideration above [36] highlighted that this is indeed the case. However, the main effect of transition for this regime is a slight alteration of viscous drag, which leaves practically unaltered blade static pressure and turbine power [36] with respect to fully turbulent boundary layers.

The excellent agreement of numerical results and experimental data shown above demonstrates the capability of the LSP-enhanced COSA code to quantitatively and reliably predict small wind turbine performance and aerodynamics, and, thus, the code suitability for the scope of the present study. Moreover, further experimental validation of COSA against the NREL Phase VI rotor at 13 m/s, reported in [21], showed a comparable level of agreement with experiments.

RESULTS

This section presents the comparative assessment of two small industrial HAWT rotors, aiming at assessing the correlation between blade design and aerodynamic performance. More specifically, the aim is to explain the qualitative and quantitative performance differences due to variations of airfoil geometry, and blade chord and twist distributions. The analyses are also aided by consideration of the available airfoil polars to demonstrate the capability of high-fidelity CFD to predict detailed aerodynamic features and their dependence on blade design. Both rotors have two blades and diameter of 13 m, and are of the downwind type, *i.e.* mounted behind the tower. Experimental data are available for one turbine only, which will be referred to as "Design 1"; the other configuration, called "Design 2", will be cross-compared with "Design 1" to investigate the relation between design variations and differences in blade aerodynamics.

The flow around the blade of each rotor was simulated at several wind speeds above the cut-in threshold of 3.5 m/s in the range 5 – 12 m/s considering straight wind conditions. Time-accurate simulations were carried out in all cases using the relative frame formulation of the governing equations. In this framework, the rotation of the rotor does not result in flow unsteadiness which, therefore, can be introduced only by the occurrence of stall. The use of periodicity boundary conditions allowed simulating the whole rotor flow using only a 180° grid sector, thus halving computational costs. The tower was not modeled, and the tower shadow effect, resulting in a 2/rev impulsive power drop due to the blades crossing the tower wake, is therefore not modeled. This omission results in a small overprediction of the rotor power, but does not affect the comparative analysis of the two rotor designs below, as it hits the performance of the two rotors in the same manner.

All CFD analyses used the novel LSP formulation discussed above, which in Section Validation was shown to be essential for obtaining high solution accuracy without adopting overly refined grids at the low flow speeds of interest in this

study. Blade boundary layers were considered fully turbulent because the level of turbulence intensity during operation of commercial turbines is expectedly substantially higher than in controlled indoor experiments like the NREL Phase VI tests, and the leading edge region often undergoes fairly rapid wear. Both factors contribute to triggering transition at the leading edge. Since the scope of the study below was to inform the industrial design of turbines developed to operate for 20 years with minimum maintenance, it was deemed more appropriate to neglect laminar-to-turbulent transition in the analyses.

All simulations featured the following parameters: oncoming air with temperature $T = 288$ K, density $\rho = 1.2259$ kg/m³, and viscosity $\mu = 1.7886 \cdot 10^{-5}$ kg/ms, and fixed rotational speed $\Omega = 56$ RPM. A constant physical time-step of $5.9 \cdot 10^{-4}$ s was used for the time-integration, as this value was found to result in solutions independent of further time-step reductions in all analyses. In all cases, simulations converged either to steady-state or a time-periodic solution.

Design 1

The radial profiles of the blade chord and twist of Designs 1 and 2 are compared in Fig. 5. The chord profiles were nondimensionalized by the maximum chord of Design 2. One notes that the blade of Design 1 has linearly tapered chord, whereas both designs feature a fairly nonlinear twist distribution. Design 1 uses airfoils of the NACA 44 series along the entire blade span.

The CFD model used for the analysis of Design 1 is depicted in Fig. 6, which also reports the adopted boundary conditions. To simplify the mesh generation process, an infinite inviscid hub was used to replace the nacelle. A structured multi-block mesh was constructed to discretize the physical domain. The grid topology features an O-grid block around the blade and four H-grid blocks, two between the O-grid and inflow and outflow boundaries, and two between the O-grid and the periodic boundaries. The O-grid past the blade sections, depicted in the top right image of Fig. 6, has 144 cells around the airfoils and 48 in the normal-like direction. The H-grid block between the O-grid block and the inflow boundary has 48 cells in the normal-like direction, whereas that between the O-grid block and the outflow boundary has 72 cells in the same direction. The other two H-grid blocks count 32 cells between the O-grid and the periodic boundaries. Beyond the tip, the grid extends radially with 56 cells up to the cylindrical far-field boundary. The blade surface is discretized with 108 cells in the radial direction, with grid spacing decreasing towards the blade tip. At the tip, the radial width of the last cell on the blade surface (that with an edge on the tip) equals the minimum distance from the airfoil in the airfoil plane itself. The

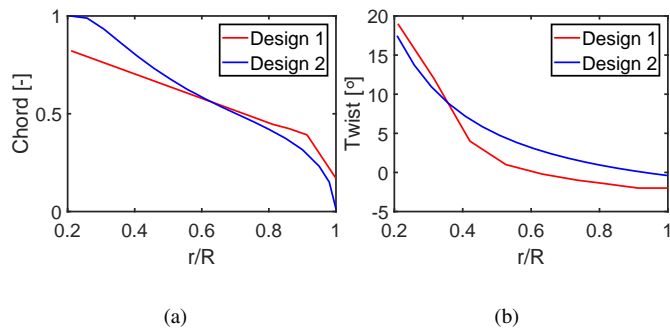


Fig. 5. Radial profiles of nondimensionalized chord (left) and twist angle (right) of Design 1 and Design 2 rotors.

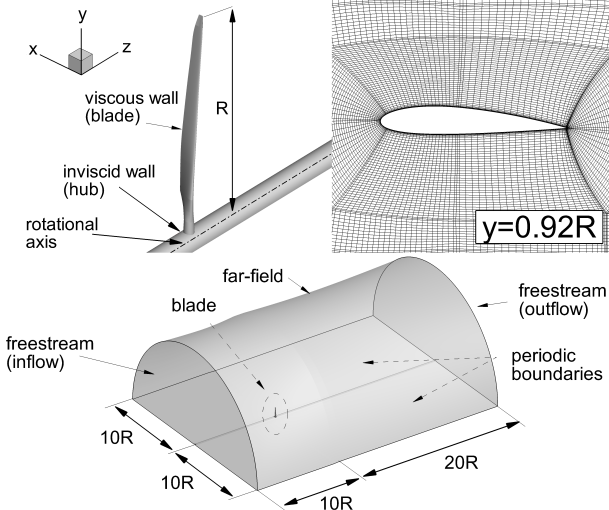


Fig. 6. Design 1 rotor: blade geometry (top left), airfoil grid at 92 % tip radius (top right), and domain dimensions and boundary conditions (bottom).

distance of the first grid point off the blade surface varies along the blade span ranging from $5 \cdot 10^{-6}$ to $8 \cdot 10^{-6}$ m, yielding $y^+ \leq 1$ around the entire blade surface. The whole mesh counts 3.75 M cells distributed into 408 blocks.

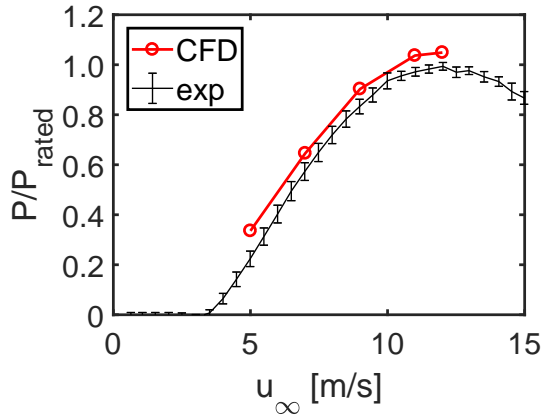


Fig. 7. Design 1: measured and computed power data.

The results of the simulations are first assessed against measured data, available only in terms of overall power. Fig. 7 compares measured and computed power curves, nondimensionalized by the measured rated power. The calculations agree well with the measurements in terms of both overall trend and quantitative data. The small overprediction of the CFD solution is consistent with the lack of modeling of the small power drop due to the tower shadow effect; moreover, simulations are performed imposing a uniform freestream velocity, whereas the field-measured power curve might also be affected by losses due to vertical wind shear. The additional validation evidence based on the comparison of measured and computed power curves indicates that reliable technical information can be extracted from COSA analyses of the rotor's aerodynamics.

The limiting streamlines on the suction side of the blade of Design 1 rotor at different wind speeds are presented in Fig. 8. One sees that the wind turbine is already stalled at the lowest considered wind speed of $u_{\infty} = 5$ m/s, as highlighted by the horizontal separation line starting at the root and extending towards the tip. Stall is stronger at the root where the blade

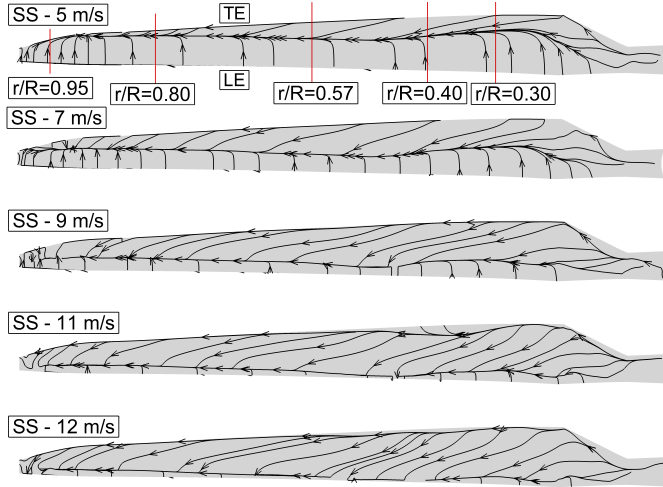


Fig. 8. Design 1: limiting streamlines on suction side at the considered wind speeds.

works with quite high angle of attack (AoA) due to low entrainment velocity. As expected, the level of stall increases rapidly as the wind speed increases, and the blade is completely stalled already at 11 m/s.

The flow features observed above were further investigated by analyzing the radial profiles of AoA for the considered wind speeds. The axial induction factor at several positions along the blade height upstream of the rotor was computed from the CFD solutions, and the relative velocity vector at the blade leading edge was evaluated using the local entrainment velocity. The spanwise distribution of AoA was determined by subtracting the local blade twist angle from the angle of the relative velocity vector on the rotor plane at each radial position. The radial profiles of Reynolds number were also evaluated using the magnitude of the relative velocity and the chord at each radial position. Figure 9 reports the spanwise distributions of AoA for all the wind speeds of interest, and it confirms the higher loading of the airfoils near the blade root. For given freestream wind speed, moving from root to tip, the entrainment velocity becomes larger than the axial wind speed component, the AoA decreases, and stall weakens in the outboard blade until it disappears for $r/R > 0.9$. Over most of the span, for given blade radius, as the freestream wind speed increases, the AoA also increases, and the separation point on the suction side moves upstream towards the leading edge, but it never reaches it, as visible in Fig. 8.

To characterize more thoroughly the blade aerodynamics of Design 1, the limiting angles of static and deep stall of its NACA 44 airfoils are considered. The static stall limit is the AoA at which the peak value of the lift coefficient occurs, whereas the deep stall limit is the AoA at which the stall separation on the suction side reaches the leading edge. In this condition, a sudden lift drop occurs, as discussed in further detail for the analysis of Design 2 below. For a given airfoil, these two limiting angles depend on the Reynolds number, and the radial profiles of this parameter for all considered wind speeds, not reported for brevity, lie within the relatively narrow range $6 - 8 \times 10^5$ for Design 1 rotor, as the increment in relative velocity at higher radii is balanced by the reduction in chord length. Using the NACA 44 polars for the Reynolds numbers of interest, one obtains the radial profiles of static and deep stall angles, also reported in Fig. 9. It is seen that the wind speed- and radial position-dependent AoA, varying in the range $9^\circ - 32^\circ$, never reaches the deep stall limit. Based on the NACA 44 polars and the CFD analyses of the operating conditions of interest, therefore, one infers that most of the

blade operates in the post-stall condition, namely above the static stall limit, for all the wind velocity of interest; however, the blade never reaches the deep stall condition. Thus, Design 1 rotor always operates with relatively high lift coefficients and achieves the required passive control by exploiting the dependence of the overall (pressure and viscous) drag coefficient on the AoA in the post-stall region.

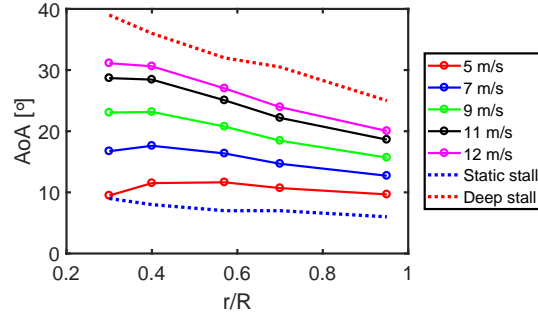


Fig. 9. Design 1: radial profiles of angle of attack for the considered wind speeds; radial profiles of static and deep stall angles derived from airfoil polars are also reported.

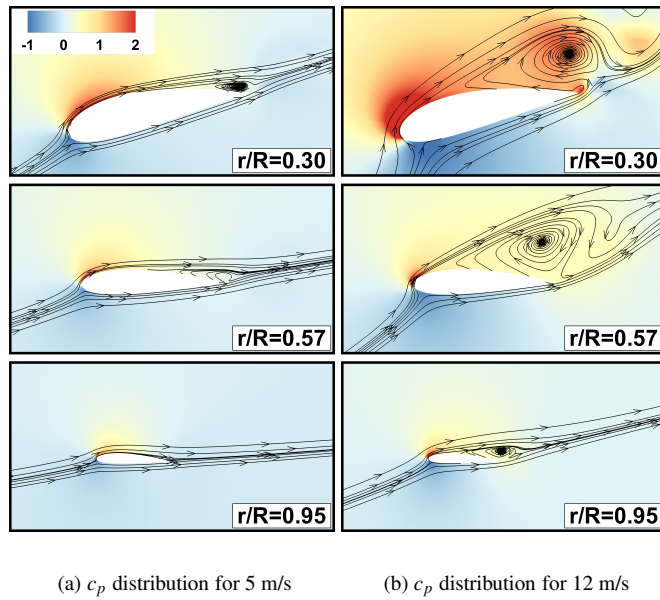


Fig. 10. Design 1: contours of static pressure coefficient and streamlines around three blade sections for wind speed of 5 m/s and 12 m/s.

The aerodynamic features discussed above are also confirmed by the blade flow patterns depicted in Fig. 10 in terms of pressure coefficient and streamlines at three spanwise positions for the highest and lowest freestream wind speeds. As expected, stall occurs at low speed in the rear part of the suction side, except for the section at $r/R = 0.95$, where stall does not occur at all. Conversely, large stalled flow regions appear at high speed, due to the larger AoA at which the blade operates, especially in the root region. However, even though the stalled region is much larger than at low wind speed, it does not reach the leading edge.

Design 2

The overall performance and the aerodynamics of the Design 2 rotor are now discussed and compared to those of Design 1. Compared to Design 1 rotor, Design 2 features overall higher tapering and twist, as depicted in Fig. 5, which highlights smaller chords and larger twist angles of Design 2 for $r/R > 0.6$ and $r/R > 0.4$ respectively. By virtue of such design, the rotor of Design 2 features lower mechanical stresses with respect to Design 1. This, however, might have a negative impact on the blade torque; in an attempt to compensate for this torque reduction, the rotor of Design 2 uses a class of profiles different from the NACA 44 series of Design 1, namely the DU airfoils: the blade of Design 2 features the DU 97 airfoil up to 30% tip radius, the DU 91 airfoil for $0.3 < r/R < 0.4$, and the DU 96 airfoil from 40% of the tip radius up to the blade tip.

All the simulations discussed below were performed with the same set-up adopted for Design 1, making use of the same physical models and numerical methods, and were run on a computational mesh constructed with the same rules.

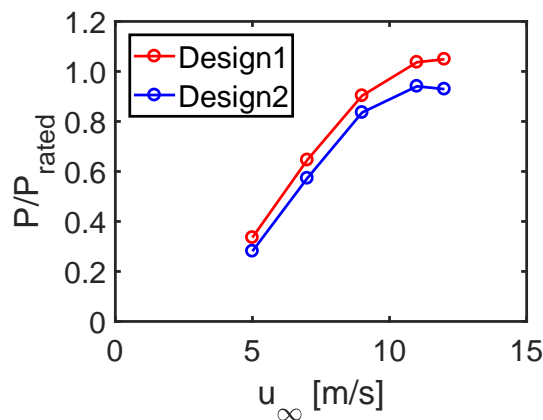


Fig. 11. Power curve of Design 1 and Design 2 rotors.

Figure 11 reports the nondimensionalized power curve of the two rotors. One first notes that Design 1 outperforms Design 2 for all considered wind speeds. However, while for wind speed in the range 5 – 9 m/s a small constant power shift is observed, probably due to the specific spanwise layout of Design 2 rotor, at the highest wind speeds the difference between the two configurations grows significantly.

To investigate the differences in rotor aerodynamics, Fig. 12 compares the spanwise distributions of the force coefficients C_N and C_T , defined respectively by Eqs. (7) and (8), of Design 1 and Design 2 at five different wind speeds. These plots show that, at low speed, the wind imparts similar aerodynamic forces on the two blade configurations, the Design 2 rotor being slightly penalized, especially for $r/R > 0.4$. This explains the lower power extracted by the rotor of Design 2 with respect to Design 1 at such low speeds. The difference between the force coefficients of the two rotors grows significantly as the velocity increases; for wind speeds of 11 and 12 m/s, the C_T profile of Design 2 does no longer decrease monotonically with the radius, and exhibits a local and severe drop in the midspan region. This effect causes the increased performance drop of Design 2 with respect to Design 1 at high speed. It is noted that this sudden loss of tangential force of Design 2 occurs around the mid part of the blade.

Figure 13 depicts the limiting streamlines on the suction side of the blade of Design 2 rotor. These plots are similar to

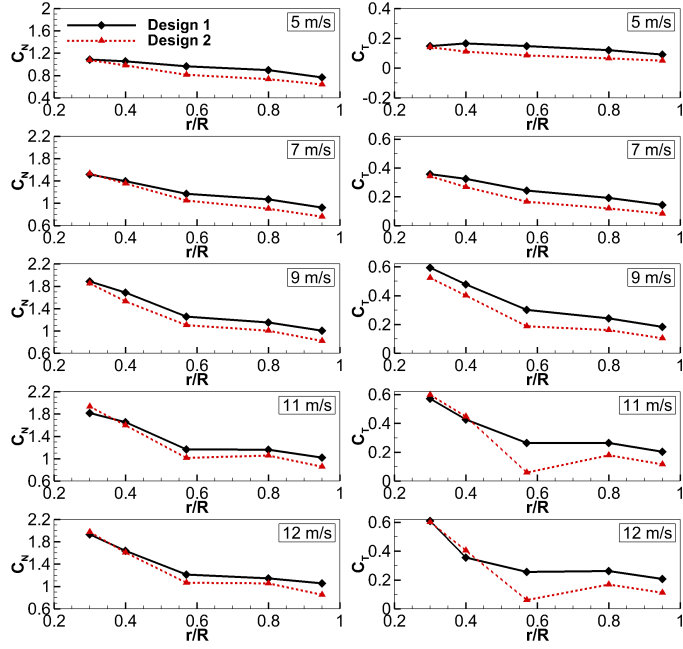


Fig. 12. Design 1 and Design 2 blade force coefficients.

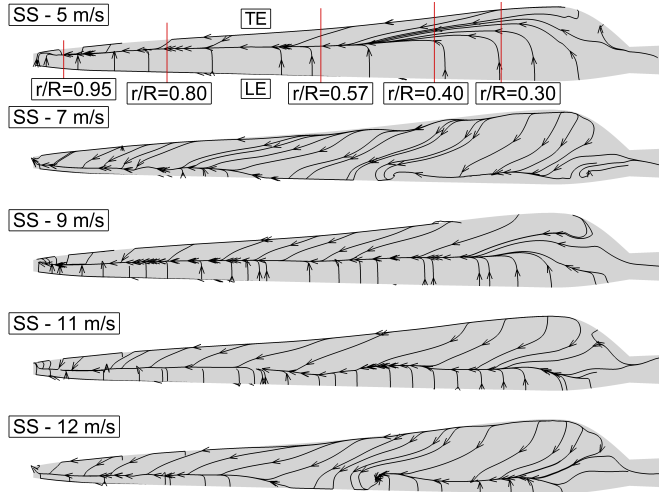


Fig. 13. Design 2: limiting streamlines on suction side at the considered wind speeds.

those of Design 1 in Fig. 8 up to 9 m/s, showing a line of separation extended along the entire blade and placed at about mid-chord. For Design 2, however, at the two highest speeds the separation line moves towards the front part of the blade and reaches the leading edge for $0.4 < r/R < 0.6$. The outcome of the sectional aerodynamic analysis of the Design 2 blade, based on the radial profiles of the AoA extracted from the CFD solutions, and the static and deep stall limiting angles determined with the polar data of the considered DU airfoils for the CFD-predicted Reynolds numbers, is reported in Fig. 14. These results help explain the aerodynamic and performance patterns observed above. At high wind speed, the AoA exceeds 22° for $0.4 < r/R < 0.6$, where the blade features the DU 96 airfoil. For the Reynolds number of operation this airfoil goes into deep stall at 22° , as shown by the DU 96 lift curve in Fig. 15. Figure 14 highlights that the onset of deep stall is a local feature at midspan of the blade of Design 2; in the root region of the blade, which operates at even higher AoA, the onset of

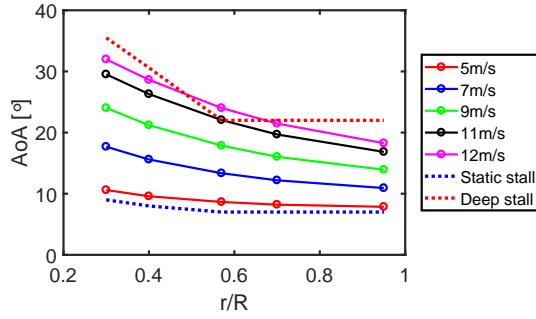


Fig. 14. Design 2: radial profiles of angle of attack for the considered wind speeds; radial profiles of static and deep stall angles derived from airfoil polars are also reported.

deep stall is avoided by the adoption of the DU 97 and DU 91 profiles, which enter deep stall for AoA exceeding 34° and 31° respectively; in the outer portion of the blade, where the DU 96 is used, the blade leaves the deep stall condition as the AoA decreases below the 22° deep stall threshold. Conversely, Design 1 does not operate in such a condition for the wind speed considered, as visible in Fig. 9.

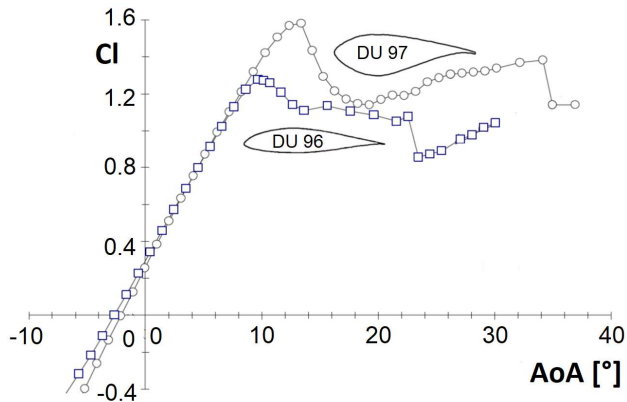


Fig. 15. Lift curves of DU profiles used by the blade of Design 2 rotor. Adapted from [37]

To complete the comparative assessment of the two turbines, the lift coefficient c_L and the drag coefficient c_D of the blade sections used by Design 1 and Design 2 rotors were extracted from the CFD simulations. The force coefficients C_N and C_T defined by Eqs. (7) and (8) were computed using the actual relative velocity vector of the wind approaching the blade leading edge area, considering also the induced velocity in the calculation of the relative velocity magnitude. These new force coefficients were then projected along the direction normal to the actual relative velocity vector to obtain c_L , and parallel this velocity vector to obtain c_D . The direction of the relative velocity vectors at the five radial positions of Design 1 and Design 2 blades are those shown in Figures 9 and 14 respectively. Then, a section-by-section percentage difference between the lift coefficients of the two rotors was calculated for each wind speed according to the relation $\Delta c_L = (c_{L,D2} - c_{L,D1})/c_{L,D1} \times 100$, and a percentage difference Δc_D was computed in a similar fashion. The variables Δc_L and Δc_D are reported in Figures 16(a) and 16(b) respectively. The Δc_L plot clearly shows that for all considered wind speeds Design 1 outperforms Design 2 at $r/R \geq 0.4$, where the DU 96 profile is employed for Design 2. For $0.3 \leq r/R \leq 0.4$ the two rotors have similar lift coefficients, with Design 2 slightly outperforming Design 1 for some wind speeds; however, this is not sufficient to compensate for the

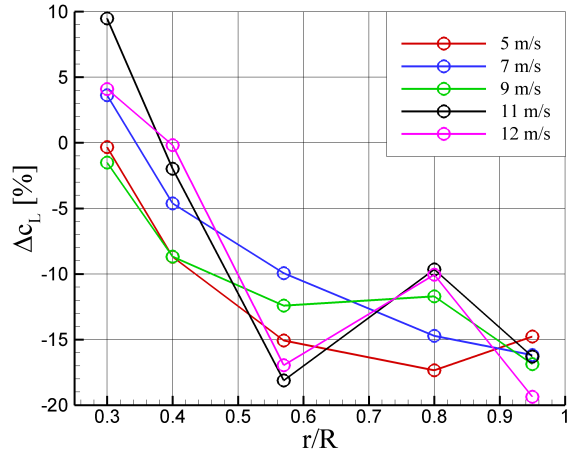
reduction of lift coefficient experienced in the outboard part of the blade. The reduced lift coefficient combined with the lower blade chord in the outboard part of the rotor contributes to the previously observed lower power of Design 2 at all wind speeds. At the highest speeds, one notes the aerodynamic effects of deep stall, which results in non-monotonic profiles caused by a sudden drop of lift coefficient for the rotor of Design 2 at $r/R = 0.57$. The patterns observed in the Δc_D plot are more irregular, and the variations of this variable are larger than those of Δc_L . In particular, in the inboard part of the rotor at $r/R \approx 0.3$ Design 2 experiences higher drag coefficient for all wind speeds, whereas the difference between the two rotors reduces significantly and becomes even negative for $r/R \geq 0.4$. At the two highest speeds the effect of deep stall manifests itself with a sudden rise of drag coefficient for the rotor of Design 2 at $r/R = 0.57$. The analysis of the aerodynamic coefficients further highlights the qualitative and quantitative effects of the onset of deep stall, helping to explain the power differences of the two turbine designs at the highest speeds. Note that even though the two blades feature slightly different chord lengths, the conclusions of the comparative analysis based on the aerodynamic force coefficients are the same as those based on the actual lift and drag forces.

The findings above are corroborated by the analysis of the flow field of three blade sections of Design 2 at the lowest and highest wind speeds considered in Fig. 17. The images highlight that the thick profiles used in the root region, even though highly loaded and featuring a severe separation on the suction side, operate in post-stall conditions but do not enter deep stall. Conversely, at mid-height the high AoA in combination with the relatively slender shape of the DU 96 profile leads to deep stall, as the flow separation reaches the leading edge.

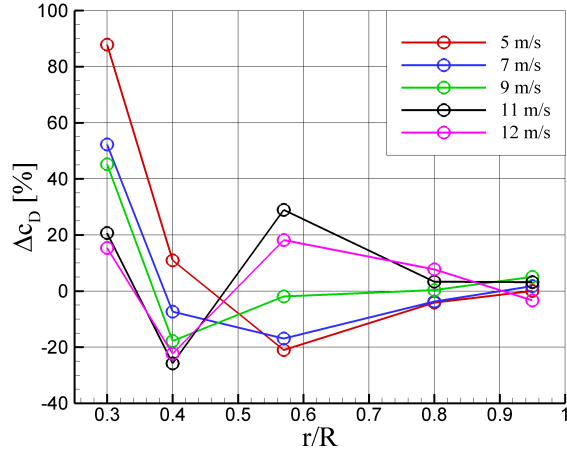
Analyses of the type reported herein allow one to characterize rotor aerodynamic designs and their critical issues. In rotor design, the selection of the blade airfoils is not straightforward, since the angle of attack is influenced by the induction factor which, in turn, depends on the aerodynamic interaction between the rotor and the wind. In conventional engineering codes, which typically use the low-fidelity BEMT model, an inherently two-dimensional (2D) approach, in conjunction with 2D airfoil force data and empirical corrections to account for 3D aerodynamic effects, the estimates of the induction factor are affected by operating condition-dependent uncertainty; the reliability of such models is likely to be insufficient for the analysis and optimal design of stall-regulated wind turbines, operating in post-stall conditions at most wind speeds. Indeed, the analyses above have shown that the aerodynamics and the power generation of these machines is extremely sensitive to the local values of the axial induction and the AoA. The prediction reliability of both parameters depends on correctly capturing the complex local 3D flow patterns associated with the stalled blade flow tri-dimensionality. Validated high-fidelity CFD systems, like the COSA code used herein, can account more reliably for complex 3D flow effects, yielding more reliable predictions of induction factors and AoAs and, more generally, complete rotor aerodynamics and performance.

CONCLUSIONS

The paper presented an investigation on the aerodynamics of small stall-controlled turbines with a high-fidelity computational flow model. The simulations, performed with the compressible density-based RANS code COSA enhanced with a novel low-speed preconditioning technique, enabled the reliable analysis of the unsteady flow due to stall, used as a passive power control system in these machines. A thorough and novel body of validation based on one of the NREL Phase VI



(a)



(b)

Fig. 16. Percentage variation of lift coefficient (left) and drag coefficient (right) of Design 2 relative to Design 1 rotor.

experiments demonstrated the reliability of the predictions achievable with COSA and the strengths of the novel LSP approach discussed in the paper. This method was shown to significantly improve the solution accuracy for a given level of grid refinement with respect to the accuracy achievable without LSP. Two industrial turbines were then analyzed and compared in a wide range of operating conditions, providing clear indications on the aerodynamics and performance of these machines. Simulations showed that the blades of both turbines operate in post-stall conditions, but a significantly higher performance drop of one of the two designs relative to the other occurred at high wind speeds due to the occurrence of deep stall. The prediction of such complex flows depends on the rotor geometry, is critical to successful turbine designs, and requires a level of fidelity not available with present design methods based on low-fidelity tools. This makes high-fidelity CFD, such as the COSA code used herein, an invaluable tool for industrial turbine design and verification.

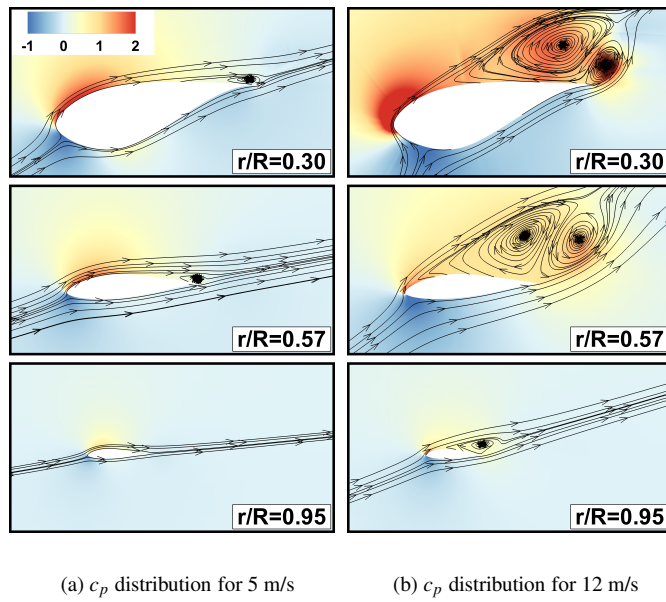


Fig. 17. Design 2: contours of static pressure coefficient and streamlines around three blade sections for wind speed of 5 m/s and 12 m/s.

Acknowledgements

The work reported herein has been supported by the UK Engineering and Physical Sciences Research Council in the framework of Lancaster University Impact Acceleration Account, Grant No. EP/R511560/1. The authors are grateful to 4navitas Ltd for their technical input to this project. All COSA CFD simulations were performed on the HEC cluster of Lancaster University, which is kindly acknowledged.

References

- [1] Forsyth, T., Burch, J., Boshell, F., and Baranowski, R., 2015. Quality Infrastructure for Renewable Energy Technologies Small Wind Turbines. Technical report, International Renewable Energy Agency.
- [2] Bortolini, B., Gamberi, M., Graziani, A., Manzini, R., and Pilati, F., 2013. “Performance and viability analysis of small wind turbines in the european union”. *Renewable Energy*, **62**, pp. 629–639.
- [3] Jain, P., 2011. *Wind Energy Engineering*. McGraw-Hill, New York, NY, USA.
- [4] Sørensen, N., Michelsen, J., and Schreck, S., 2002. “Navier-Stokes Predictions of the NREL Phase VI Rotor in the NASA Aimes 80 ft × 120 ft Wind Tunnel”. *Wind Energy*, **5**, pp. 151–169.
- [5] Potsdam, M., and Mavriplis, D., 2009. Unstructured Mesh CFD Aerodynamic Analysis of the NREL Phase VI Rotor. AIAA paper 2009-1221, January. 47th AIAA Aerospace Sciences Meeting Including The New Horizons Forum and Aerospace Exposition, Orlando, Florida.
- [6] Bechmann, A., Sorensen, N., and Zahle, F., 2011. “CFD simulations of the MEXICO rotor”. *Wind Energy*, **14**, pp. 677–689.
- [7] Mo, J.-O., Choudhry, A., Arjomandi, M., and Lee, Y.-H., 2013. “Large eddy simulation of the wind turbine wake characteristics in the numerical wind tunnel model”. *Journal of Wind Engineering and Industrial Aerodynamics*, **112**,

- pp. 11–24.
- [8] Simms, D., Schreck, S., Hand, M., and Fingersh, L., 2001. NREL Unsteady Aerodynamics Experiment in the NASA-Ames Wind Tunnel: A Comparison of Predictions to Measurements. Tech. Rep. NREL/TP-500-29494, NREL, Golden, CO, USA, June.
- [9] Hand, M. M., Simms, D. A., Fingersh, L. J., Jager, D. W., Cotrell, J. R., Schreck, S., and Larwood, S. M., 2001. Unsteady Aerodynamics Experiment Phase VI: Wind Tunnel Test Configurations and Available Data Campaigns. Tech. Rep. NREL/TP-500-29955, NREL, Golden, CO, USA, Dec.
- [10] Snel, H., Schepers, J., and Montgomerie, B., 2007. “The MEXICO project (Model Experiments in Controlled Conditions): The database and first results of data processing and interpretations”. *Journal of Physics: Conference Series*, **75**.
- [11] Gerhard, T., Sturm, M., and Carolus, T., 2013. Small Horizontal Axis Wind Turbine: Analytical Blade Design and Comparison with RANS-prediction and First Experimental data. ASME paper GT2013-94158, June.
- [12] Campobasso, M., Piskopakis, A., Drofelnik, J., and Jackson, A., 2013. “Turbulent Navier-Stokes Analysis of an Oscillating Wing in a Power-Extraction Regime Using the Shear Stress Transport Turbulence Model”. *Computers and Fluids*, **88**, December, pp. 136–155.
- [13] Menter, F., 1994. “Two-equation Turbulence-models for Engineering Applications”. *AIAA Journal*, **32**(8), August, pp. 1598–1605.
- [14] Campobasso, M., Yan, M., Bonfiglioli, A., Gigante, F., Ferrari, L., Balduzzi, F., and Bianchini, A., 2018. “Low-speed preconditioning for strongly coupled integration of Reynolds-averaged Navier-Stokes equations and two-equation turbulence models”. *Aerospace Science and Technology*, **77**, pp. 286–298.
- [15] Chen, J., Ghosh, A., Sreenivas, K., and Whitfield, D., 1997. Comparison of computations using Navier-Stokes equations in rotating and fixed coordinates for flow through turbomachinery. 35th Aerospace Sciences Meeting and Exhibit, January. Reno, NV, U.S.A.
- [16] Campobasso, M., and Drofelnik, J., 2012. “Compressible Navier-Stokes analysis of an oscillating wing in a power-extraction regime using efficient low-speed preconditioning”. *Computers and Fluids*, **67**, August, pp. 26–40.
- [17] Drofelnik, J., and Campobasso, M., 2016. “Comparative Turbulent Three-Dimensional Navier-Stokes Hydrodynamic Analysis and Performance Assessment of Oscillating Wings for Renewable Energy Applications”. *International Journal of Marine Energy*, **16**, pp. 100–115.
- [18] Balduzzi, F., Bianchini, A., Gigante, F., Ferrara, G., Campobasso, M., and Ferrari, I., 2015. Parametric and Comparative Assessment of Navier-Stokes CFD Technologies for Darrieus Wind Turbines Performance Analysis. ASME paper GT2015-42663, June.
- [19] Balduzzi, F., Drofelnik, J., Bianchini, A., Ferrara, G., Ferrari, I., and Campobasso, M., 2017. “Darrieus wind turbine blade unsteady aerodynamics: a three-dimensional Navier-Stokes CFD assessment”. *Energy*, **128**, pp. 550–563.
- [20] Balduzzi, F., Marten, D., Bianchini, A., Drofelnik, J., Ferrari, I., Campobasso, M., Pechlivanoglou, G., Nayari, C., Ferrara, G., and Paschereit, C., 2018. “Three-Dimensional Aerodynamic Analysis of a Darrieus Wind Turbine Blade

- Using Computational Fluid Dynamics and Lifting Line Theory”. *Journal of Engineering for Gas Turbines and Power*, **140**(2).
- [21] Drofelnik, J., Da Ronch, A., and Campobasso, M., 2018. “Harmonic balance Navier-Stokes aerodynamic analysis of horizontal axis wind turbines in yawed wind”. *Wind Energy*, **21**(7), pp. 515–530. DOI: 10.1002/we.2175.
- [22] Campobasso, M., Sanvito, A., Drofelnik, J., Jackson, A., Zhou, Y., Xiao, Q., and Croce, A., 2018. Compressible Navier-Stokes Analysis of Floating Wind Turbine Rotor Aerodynamics. ASME paper IOWTC2018-1059, November.
- [23] Venkatakrishnan, V., 1991. “Preconditioned Conjugate Gradient Methods for the Compressible Navier-Stokes Equations”. *AIAA Journal*, **29**(7), pp. 1092–1100.
- [24] Obayashi, S., 1992. “Freestream capturing for moving coordinates in three dimensions”. *AIAA Journal*, **30** (4), pp. 1125 – 1128.
- [25] Campobasso, M., and Baba-Ahmadi, M., 2012. “Analysis of Unsteady Flows Past Horizontal Axis Wind Turbine Airfoils Based on Harmonic Balance Compressible Navier-Stokes Equations with Low-Speed Preconditioning”. *Journal of Turbomachinery*, **134**(6), November.
- [26] Campobasso, M., Gigante, F., and Drofelnik, J., 2014. Turbulent Unsteady Flow Analysis of Horizontal Axis Wind Turbine Airfoil Aerodynamics Based on the Harmonic Balance Reynolds-Averaged Navier-Stokes Equations. ASME paper GT2014-25559, June.
- [27] Campobasso, M., Drofelnik, J., and Gigante, F., 2016. “Comparative Assessment of the Harmonic Balance Navier-Stokes Technology for Horizontal and Vertical Axis Wind Turbine Aerodynamics”. *Computers and Fluids*, **136**, pp. 345–370.
- [28] Jackson, A., Campobasso, M., and Drofelnik, J., 2018. “Load balance and parallel I/O: Optimising COSA for large simulations”. *Computers and Fluids*, March.
- [29] Jackson, A., and Campobasso, M., 2011. “Shared-memory, Distributed-memory and Mixed-mode Parallelization of a CFD Simulation Code”. *Computer Science Research and Development*, **26**(3-4), pp. 187–195.
- [30] Turkel, E., 1987. “Preconditioned methods for solving the incompressible and low speed compressible equations”. *Journal of Computational Physics*, **72**, pp. 277–298.
- [31] Weiss, J., and Smith, W., 1995. “Preconditioning applied to variable and constant density flows”. *AIAA Journal*, **33**(11), pp. 2050–2057.
- [32] Campobasso, M., Yan, M., Drofelnik, J., Piskopakis, A., and Caboni, M., 2014. Compressible Reynolds-Averaged Navier-Stokes Analysis of wind Turbine Turbulent Flows Using a Fully Coupled Low-Speed Preconditioned Multigrid Solver. ASME paper GT2014-25562, June.
- [33] Campobasso, M., and Baba-Ahmadi, M., 2011. “Ad-hoc Boundary Conditions for CFD Analyses of Turbomachinery Problems with Strong Flow Gradients at Farfield Boundaries”. *Journal of Turbomachinery*, **133**(4), October.
- [34] Drofelnik, J., 2017. “Massively Parallel Time- and Frequency-Domain Navier-Stokes Computational Fluid Dynamics Analysis of Wind Turbines and Oscillating Wing Unsteady Flows”. PhD thesis, Glasgow University, United Kingdom, June.

- [35] Sorensen, N. N., Michelsen, J. A., and Shreck, S., 2002. “Navier Stokes Predictions of the NREL Phase VI Rotor in the NASA Ames 80 ft x 120 ft Wind Tunnel”. *Wind Energy*, **5**, pp. 151–169.
- [36] Sørensen, N., 2009. “CFD Modelling of Laminar-Turbulent Transition for Airfoils and Rotors Using the $\gamma - \tilde{R}e_0$ Model”. *Wind Energy*, **12**, pp. 715–733.
- [37] Timmer, W., and van Rooij, R., 2001. “Some Aspects of High Angle-of-Attack Flow on Airfoils for Wind Turbine Application”. In Proceedings of the European conference on Wind Energy, Copenhagen, pp. 355–358.